NRC Publications Archive (NPArC)
Archives des publications du CNRC (NPArC)

Ab initio constrained crystal-chemical Rietveld refinement of Ca10(VxP1-xO4)6F2 apatites

Mercier, Patrick H.J.; Dong, Zhili; Baikie, Thomas; Le Page, Yvon; White, T. J.; Whitfield, Pamela S.; Mitchell, Lyndon

Web page / page Web

http://dx.doi.org/10.1107/S0108768106045538
http://nparc.cisti-icist.nrc-cnrc.gc.ca/npsi/ctrl?action=rtdoc&an=14146327&lang=en
http://nparc.cisti-icist.nrc-cnrc.gc.ca/npsi/ctrl?action=rtdoc&an=14146327&lang=fr

National Research Council Canada
Conseil national de recherches Canada

Ab initio constrained crystal-chemical Rietveld refinement of $Ca_{10}(V_xP_{1-x}O_4)_6F_2$ apatites

Patrick H. J. Mercier,[a]* Zhili Dong,[b] Thomas Baikie,[b] Yvon Le Page,[a] T. J. White,[b] Pamela S. Whitfield[a] and Lyndon D. Mitchel[c]

[a]Institute for Chemical Process and Environmental Technology (ICPET), National Research Council of Canada, Ottawa, Ontario, Canada K1A 0R6, [b]School of Materials Science and Engineering, Nanyang Technological University, Singapore 639798, Singapore, and [c]Institute for Research in Construction (IRC), National Research Council of Canada, Ottawa, Ontario, Canada K1A 0R6

Correspondence e-mail:
patrick.mercier@nrc-cnrc.gc.ca

Extraction of reliable bond distances and angles for $Ca_{10}(V_xP_{1-x}O_4)_6F_2$ apatites using standard Rietveld refinement with Cu $K\alpha$ X-ray powder data was significantly impaired by large imprecision for the O-atom coordinates. An initial attempt to apply crystal-chemical Rietveld refinements to the same compounds was partly successful, and exposed the problematic determination of two oxygen–metal–oxygen angles. Ab initio modeling with VASP in space groups $P6_3/m$, $P2_1/m$ and Pm showed that both these angular parameters exhibited a linear dependence with the vanadium content. Stable crystal-chemical Rietveld refinements in agreement with quantum results were obtained by fixing these angles at the values from ab initio simulations. Residuals were comparable with the less precise standard refinements. The larger vanadium ion is accommodated primarily by uniform expansion and rotation of BO_4 tetrahedra combined with a rotation of the Ca–Ca–Ca triangular units. It is proposed that the reduction of symmetry for the vanadium end-member is necessary to avoid considerable departures from formal valences at the A^{II} and B sites in $P6_3/m$. The complementarity of quantum methods and structural analysis by powder diffraction in cases with problematic least-squares extraction of the crystal chemistry is discussed.

1. Introduction

Apatite-type structures combine crystallochemical flexibility with considerable durability, making them materials of interest for the long-term stabilization of toxic metals from municipal incinerators (Eighmy et al., 1998; Valsami-Jones et al., 1998; Crannell et al., 2000) and high-level nuclear waste (Ewing & Wang, 2002; Vance et al., 2003; Terra et al., 2006). The most common symmetry is $P6_3/m$, leading to the general formula $[A_4^I][A_6^{II}][(BO_4)_6]X_2$, although numerous low-symmetry derivatives have been reported. Topologically, apatites can be considered to be one-dimensionally microporous and zeolite-like, with a flexible framework created through the corner-connection of A^IO_6 metaprism columns with isolated BO_4 tetrahedra. The channels are occupied by A^{II} ions in the disposition of irregular $A^{II}O_6X$ polyhedra. A and B cation ordering is observed on occasion and usually leads to a reduction of symmetry.

In solid solution fluorapatite $[Ca_{10}(PO_4)_6F_2]$ can accommodate larger ions of valence 1+, 2+ and 3+ in place of Ca, and smaller 4+, 5+ and 6+ ions for P (White et al., 2005). While apatites have the potential to immobilize a spectrum of elements, compositional tailoring is nevertheless required, as their adaptability is constrained to suitable combinations of ions that maintain charge balance and accept the steric and topological limitations of the structure. A model involving

37

Table 1
Instrument parameters used for X-ray powder diffraction Rietveld refinement.

Geometry: Bragg–Brentano	Divergence slit: fixed = 1.0°
Radiation source: Cu $K\alpha$	Receiving slit: 0.3 mm
Generator: 40 kV, 40 mA	Detector: scintillation counter
Tube: 12 mm long line focus	Step size: 0.02°
Scan mode: $\theta/2\theta$	Time per step: 10 s
Secondary monochromator: graphite	Angular range: 10–140° 2θ
Primary and secondary Soller slits: 6.0°	Mean temperature of measurement: ~ 295 K

Table 2
Summary of the parameters refined and derived for crystal-chemical (C-CH) and standard crystallographic (CRYS) refinement models.

Please refer to Table 1 in Mercier, Le Page *et al.* (2005) for all the parameter definitions and symbols, as well as all the equations necessary to obtain the parameters derived from those that are refined.

	C-CH	CRYS
Parameters refined	$d_{A^{\mathrm{I}}-\mathrm{O}1}$, $\Delta_{A^{\mathrm{I}}-\mathrm{O}}$, $\delta_{A^{\mathrm{I}}}$, $\alpha_{A^{\mathrm{I}}}$, $d_{B-\mathrm{O}}$, $\tau_{\mathrm{O}-B-\mathrm{O}}$, $\rho_{A^{\mathrm{II}}}$, $\alpha_{A^{\mathrm{II}}}$, $d_{A^{\mathrm{II}}-\mathrm{O}3}$, $\varphi_{\mathrm{O}3-A^{\mathrm{II}}-\mathrm{O}3}$ (Total = 10)	a, c, $A^{\mathrm{I}}z$, $A^{\mathrm{II}}x$, $A^{\mathrm{II}}y$, Bx, By, O1x, O1y, O2x, O2y, O3x, O3y, O3z (Total = 14)
Parameters derived	a, c, $\psi_{A^{\mathrm{I}}-\mathrm{O}1}$, η, $A^{\mathrm{I}}z$, $A^{\mathrm{II}}x$, $A^{\mathrm{II}}y$, Bx, By, O1x, O1y, O2x, O2y, O3x, O3y, O3z	$(A^{\mathrm{I}}-\mathrm{O}1)$, $(A^{\mathrm{I}}-\mathrm{O}1)^{A^{\mathrm{I}}z=0}$, $\Delta_{A^{\mathrm{I}}-\mathrm{O}}$, $\Delta_{A^{\mathrm{I}}-\mathrm{O}}^{A^{\mathrm{I}}z=0}$, $\delta_{A^{\mathrm{I}}}$, $\alpha_{A^{\mathrm{I}}}$, $\langle B-\mathrm{O}\rangle$, $\langle\tau_{\mathrm{O}-B-\mathrm{O}}\rangle$, $\rho_{A^{\mathrm{II}}}$, $(A^{\mathrm{II}}-X)$, $\alpha_{A^{\mathrm{II}}}$, $(A^{\mathrm{II}}-\mathrm{O}3)$, $\varphi_{\mathrm{O}3-A^{\mathrm{II}}-\mathrm{O}3}$, $\psi_{A^{\mathrm{I}}-\mathrm{O}1}^{A^{\mathrm{I}}z=0}$

crystal chemical parameterization (Mercier, Le Page *et al.*, 2005) was then implemented in scripts (Mercier *et al.*, 2006a) for Rietveld refinement with powder diffraction data using *TOPAS* (Bruker, 2005) with the goal of facilitating the design of eco-apatites as storage matrices. This approach has been complemented through the systematic exploration of apatite domains by the synthesis of a wide variety of substituted compounds (Dong *et al.*, 2002; Dong & White, 2004a,b; Kim *et al.*, 2005).

In this paper it is demonstrated that precise crystallographic information can be extracted from the X-ray diffraction profiles of vanadium-substituted fluorapatites (also known as fluorovanadinites) through constraining of the crystal-chemical refinement with the results of quantum mechanical optimization.

2. Experimental

2.1. Sample synthesis and characterization

Eleven apatite powders of the $Ca_{10}(V_xP_{1-x}O_4)_6F_2$ solid-solution series ($x = 0.0, 0.1, \ldots, 1.0$) were synthesized *via* solid-state chemical reaction. CaO (obtained by firing and decomposing AR-grade $CaCO_3$ at 1173 K), V_2O_5 and CaF_2 powders were mixed with dilute orthophosphoric acid in stoichiometric proportions and stirred at room temperature for more than 2 h. The sludge was dried at 368 K in an oven for 2 d, followed by heat treatment at 1173 K for 24 h. Detailed examination of the samples by scanning electron microscopy, energy-dispersive X-ray spectroscopy and mineralogical observation with a polarizing microscope were consistent with complete reaction. We accordingly assumed compositions for the samples from the proportions of the reactants before synthesis.

2.2. Electron diffraction and imaging

An extensive search of all $Ca_{10}((V_xP_{1-x})O_4)_6F_2$ materials was initiated by transmission electron microscopy (TEM) using a JEM-3010 instrument operated at 300 keV. For each sample, a small quantity of fluorovanadinite was lightly crushed under ethanol with an agate mortar and pestle, then dispersed ultrasonically. Several drops of the suspension were deposited on holey-carbon coated copper grids and the crystal fragments oriented perpendicular to the tunnel direction to search for V/P order.

2.3. X-ray powder diffraction

Powder diffraction patterns were collected with a Shimadzu LabX XRD-6000 diffractometer (Bragg–Brentano geometry) equipped with a Cu $K\alpha$ X-ray tube operated at 40 kV and 40 mA (Table 1). Samples were mounted in a top-loaded trough and were not rotated during data collection. Under these conditions the intensity of the strongest peak was 10 000–12 000 counts. Patterns for samples of the 11 compositions prepared in §2.1 were analyzed. Very minor impurity reflections of $Ca_3(PO_4)_2$ and/or $Ca_3(VO_4)_2$ were detected in the diffractograms for samples of nominal compositions $Ca_{10}(PO_4)_6F_2$, $Ca_{10}(V_{0.1}P_{0.9}O_4)_6F_2$ and $Ca_{10}(V_{0.9}P_{0.1}O_4)_6F_2$. All apatite
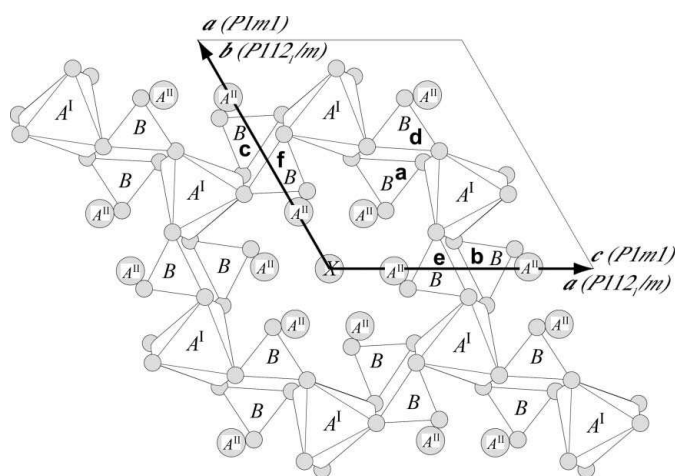

Figure 1
Illustration of the six possible atomic sites for the location of V atoms in $P2_1/m$ and Pm model structures.
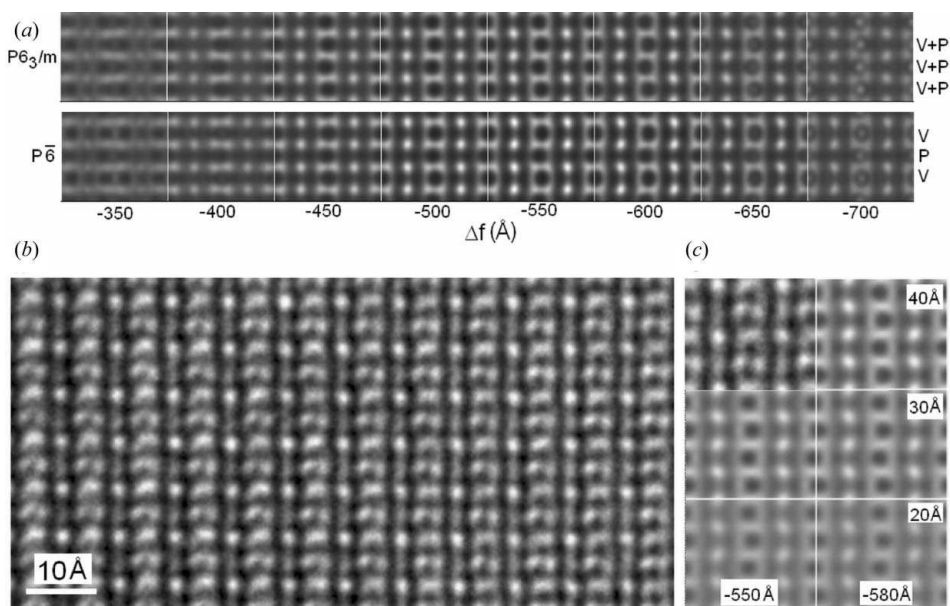
Figure 2
(a) A [100] through-focal series for disordered $P6_3/m$ and ordered vanadium and phosphorus models of $Ca_{10}((V_{0.5}P_{0.5})O_4)_6F_2$ calculated for a thickness of 47 Å using the multislice method as realised in *JEMS* (Stadelmann, 1987). Structures derived from X-ray determinations were used for the calculations. Microscope parameters were C_s = 1.4 mm, spread of focus = 10 nm, beam semi-convergence = 0.5 mrad. (b) A high-resolution image of a region in a crystal of nominal composition $Ca_{10}((V_{0.5}P_{0.5})O_4)_6F_2$. Such images, which extended for many thousands of Ås, were characteristic of the crystals over the entire solid solution, indicating an absence of miscibility gaps that would promote the formation of phosphorous- or vanadium-rich nanodomains. (c) Comparison of the experimental and calculated images of the $P2_1/m$ model of $Ca_{10}(VO_4)_6F_2$ (Dong & White, 2004b). The small departure from the hexagonal metric could not be distinguished in such images, but was apparent in selected-area diffraction patterns.

Two types of Rietveld refinement modeling were used (Table 2):

(i) a standard crystallographic approach in $P6_3/m$ involving 14 crystallographic parameters (lattice parameters a and c, 12 fractional atomic coordinates);

(ii) a crystal-chemical determination where 10 parameters representing observed polyhedral distortions are directly refined by least-squares refinement (Mercier, Le Page *et al.*, 2005; Mercier *et al.*, 2006a).

The F atoms were assumed to occupy a Wyckoff position of type 2(a) in $P6_3/m$ (x, y, z = 0, 0, 1/4; 0, 0, 3/4) for all refinements. In view of the compositional homogeneity observed in §2.1, occupancy factors were fixed at the nominal values of $Ca_{10}(V_xP_{1-x}O_4)_6F_2$, while refining only the isotropic atomic displacement parameters (ADPs). A common isotropic ADP was assumed for the O1, O2 and O3 sites (beqO), whereas individual isotropic ADPs were refined for the A^I, A^{II} and B cation sites (beqA1, beqA2, beqB; Table 2). On the basis of singular value decomposition (SVD) analyses of the least-squares normal-equations matrix performed using the program *SVDdiagnostic* (Mercier *et al.*, 2006b), these two types of Rietveld refinement schemes were shown to have similar numerical stability for a high-quality X-ray powder data set of the fluorapatite end-member $Ca_{10}(PO_4)_6F_2$ in Mercier *et al.* (2006a).

reflections could be assigned to $P6_3/m$ symmetry, except for the vanadium end-member where split peaks were indicative of lower symmetry.

2.4. Rietveld analysis

The software program *TOPAS*, Version 3.0 (Bruker, 2005), implementing the fundamental parameters approach (FPA; Cheary & Coelho, 1992) was used for Rietveld refinement. In the convolution-based profile-fitting process of the FPA (Kern *et al.*, 2004), the intensity profile is synthesized from the X-ray emission profile, the instrument parameters and specimen-dependent parameters. In addition to the integrated intensities and 2θ positions of the diffraction lines, both diffractometer- and specimen-dependent parameters may be refined, and constitute the convolution parameters that are used to generate the aberration profiles. In the present work a common set of diffractometer-dependent variables (Table 1) were used with a full axial divergence model (Cheary & Coelho, 1998a,b). The specimen-dependent parameters which were refined were the zero error, a user-specified number of coefficients of a Chebyshev polynomial fitting the background, and the 'Crystallite Size' and/or 'Microstrain' parameters used to model microstructure-controlled line broadening.

2.5. *Ab initio* modeling

The modeling and *ab initio* interface software environment *Materials Toolkit*, Version 2.0 (Le Page & Rodgers, 2005; http://www.tothcanada.com/toolkit/), was used to prepare input files for *ab initio* total-energy minimization calculations. The crystallographic parameters arising from these calculations for $P6_3/m$ apatite end-member compositions $Ca_{10}(PO_4)_6F_2$ and $Ca_{10}(VO_4)_6F_2$ were reported earlier (Mercier, Le Page *et al.*, 2005; Mercier, Whitfield *et al.*, 2005) and are listed in Table 3 (supplementary material[1]). To model

[1] Supplementary data for this paper are available from the IUCr electronic archives (Reference: KD5006). Services for accessing these data are described at the back of the journal.
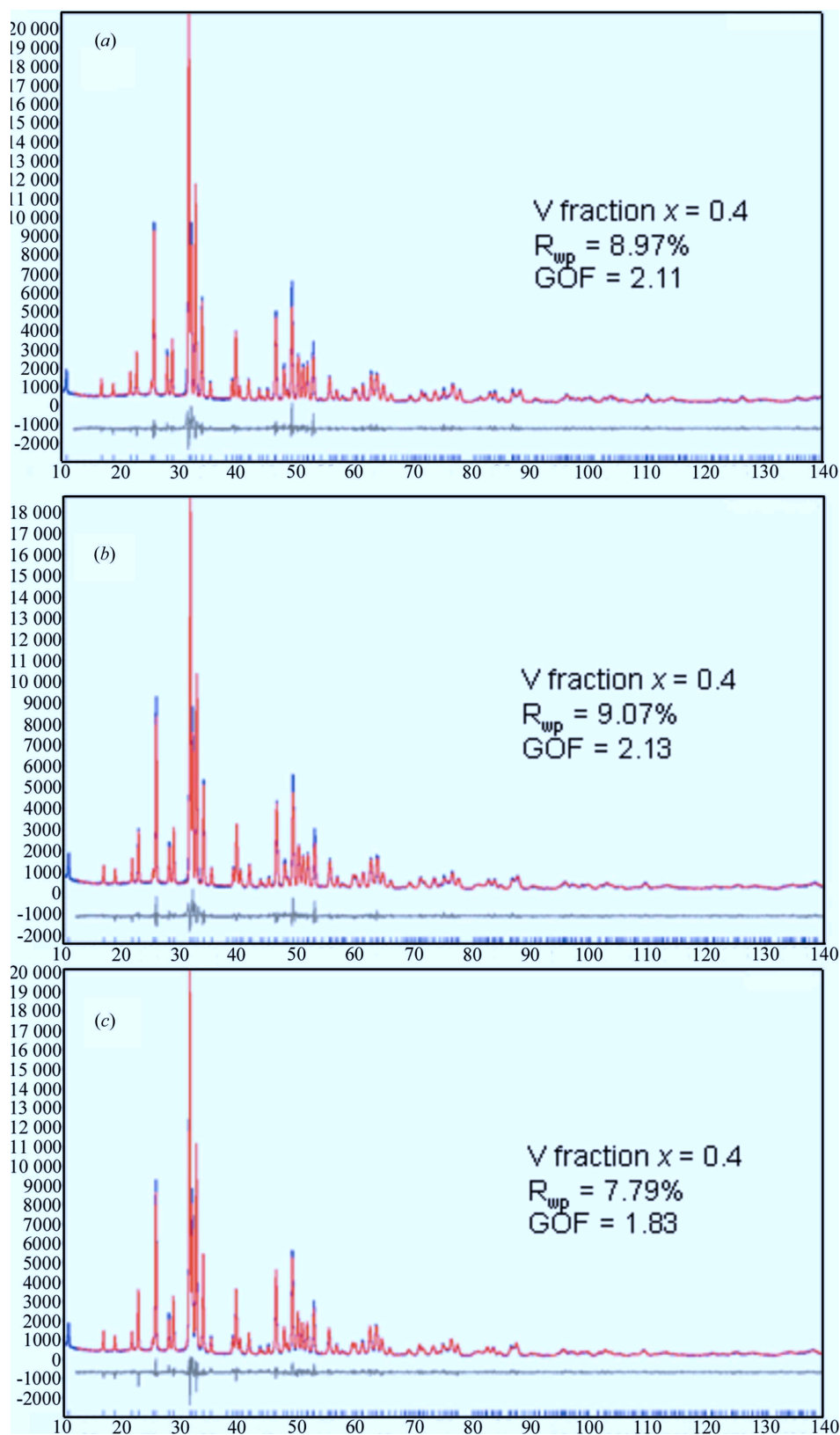
Figure 3
Typical profile fits obtained for the different types of Rietveld refinement: (a) unrestrained and (b) restrained standard crystallographic refinement; (c) crystal-chemical refinement.

the solid-solution series, coordinate-only (CO) optimizations using experimental lattice parameters (Table 4 – see supplementary material) and cell-and-coordinate (CC) optimizations for materials with ideal compositions $Ca_{10}(V_{1/6}P_{5/6}O_4)_6F_2$, $Ca_{10}(V_{2/6}P_{4/6}O_4)_6F_2$, $Ca_{10}(V_{3/6}P_{3/6}O_4)_6F_2$ and $Ca_{10}(V_{4/6}P_{2/6}O_4)_6F_2$ were performed. Modeling for solid solutions began with a description in the space group $P1$ of the $P6_3/m$ structure of $Ca_{10}(PO_4)_6F_2$. In this $P1$ model now containing six independent P atoms, we replaced the required proportion of P atoms by vanadium ones. This gave five ordered structures that we used as models for the corresponding solid solutions. Automated extraction of the symmetry of the V compounds by *Materials Toolkit* indicated the space group $P2_1/m$ when there was an even number of V atoms per cell [*e.g.* $Ca_{10}(VO_4)_2(PO_4)_4F_2$] and Pm for the remainder (Fig. 1). For direct comparison of coordinates with previous work (Dong & White, 2004b), the b-unique $P2_1/m$ setting was transformed into the c-unique $P112_1/m$ setting, before proceeding with *ab initio* optimization. The lattice parameters used for CO optimizations were those determined experimentally for samples with nominal compositions closest to the ideal compositions used in the *ab initio* models for solid solutions; *e.g.* the experimental lattice parameters for the sample $Ca_{10}(V_{0.3}P_{0.7}O_4)_6F_2$ (Table 4 – see supplementary material) was used for CO optimization of the $P112_1/m$ model with the composition $Ca_{10}(V_{2/6}P_{4/6}O_4)_6F_2$ (Table 3b – supplementary material).

VASP (Kresse, 1993; Kresse & Hafner, 1993, 1994) was used for all *ab initio* calculations with the following common execution parameters: GGA PAW potentials (Kresse & Joubert, 1999); electronic convergence at 1×10^{-7} eV; convergence for forces of 1×10^{-4} eV Å^{-1}; Davidson-

blocked iterative optimization of the wavefunctions in combination with reciprocal-space projectors (Davidson, 1983); reciprocal space integration with a Monkhorst–Pack scheme (Monkhorst & Pack, 1976); a Methfessel–Paxton smearing scheme of the order 1 and width 0.2 eV for energy corrections (Methfessel & Paxton, 1989). Spin polarization corrections were not used. K-mesh dimensions of $2 \times 2 \times 3$ and $2 \times 3 \times 2$ were employed for $P112_1/m$ and $P1m1$ models, respectively (Table 3 – supplementary material). A total of 20 to 35 single-point energy-minimization iterations were completed for each simulation to ensure proper convergence of atom relaxation, calculated energy and stress. The calculations required approximately 2 d per structure on a single 3 gHz Athlon-64 PC running serial $VASP$4.6.3 under Microsoft® $Windows$® XP, using the execution scheme described above. The resulting atomic coordinates and cell parameters are summarized in Table 3 (supplementary material), together with the total free-energy output for the final mini-mization cycles of each simulation.

3. Results

3.1. Electron diffraction and imaging

Models computed through the focal series for the [100] zone axis of $P6_3/m$ and $P\bar{6}$ for $Ca_{10}((V_{0.5}P_{0.5})O_4)_6F_2$ are shown as the top and the bottom bands of Fig. 2(a), respectively. The high-resolution image shown in Fig. 2(b) is a typical example of a structure projection along [100] for the preparation with the nominal composition $Ca_{10}((V_{0.5}P_{0.5})O_4)_6F_2$. In Fig. 2(c) a [100] high-resolution picture for $Ca_{10}(VO_4)_6F_2$ is compared with simulated images using the $P2_1/m$ model proposed earlier by Dong & White (2004b).

3.2. Extraction of crystal chemistry by standard Rietveld refinement

Unrestrained and restrained standard Riet-veld refinements were performed for all compositions except the vanadium end-member (Table 4 – supplementary material). Typical profile fits are shown in Fig. 3. The restraints were implemented by applying the 'Parabola_N' penalty function of $TOPAS$ so that the B-site cations were soft-constrained to a distance $r_o = 1.54 + (1.74 - 1.54)x$ Å away from their four nearest-neighbor O atoms, the values being selected on the basis of the standard ionic radii (Shannon, 1976). Table 5 (supplementary material) summarizes the crystal-chemical parameters extracted from standard Rietveld refinement results (Table 4 – supplementary material) using the equations given in Table 1(b) of Mercier, Le Page et al.
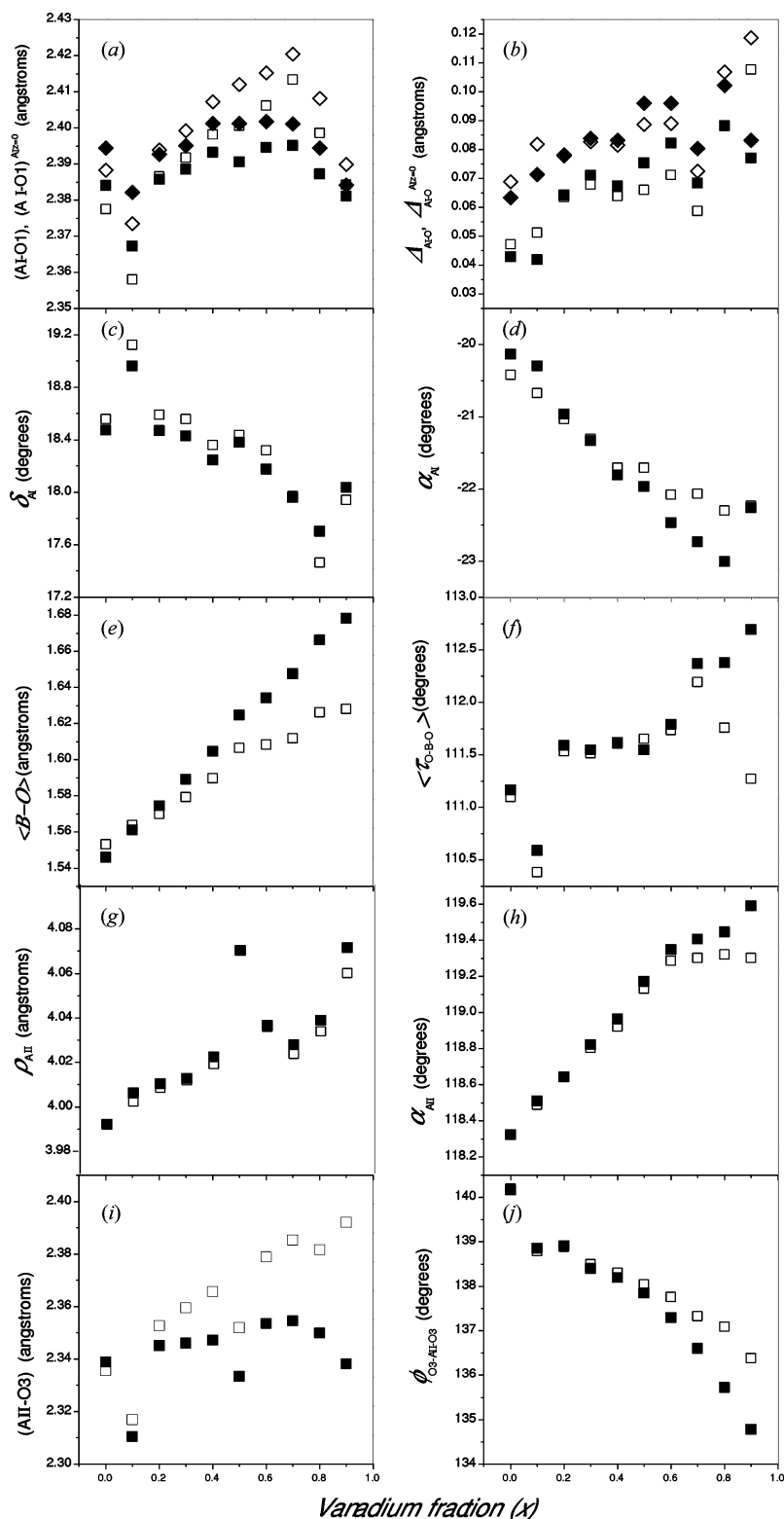

Figure 4
Crystal-chemical parameters extracted from unrestrained (open symbols) and restrained (filled symbols) standard Rietveld refinement results (Table 4 – see supplementary material) using the equations given in Table 1(b) of Mercier, Le Page *et al.* (2005).

(2005). Fig. 4 plots these indirectly determined crystal-chemical parameters obtained by the analysis of fractional atomic coordinates and lattice parameters (Table 4 – see supplementary material) as a function of the vanadium fraction x. It is apparent that, as far as the extraction of the crystal chemistry is concerned, unrestrained *versus* restrained standard refinements show approximately the same overall variation of parameter values and systematic trends across the solid-solution series.
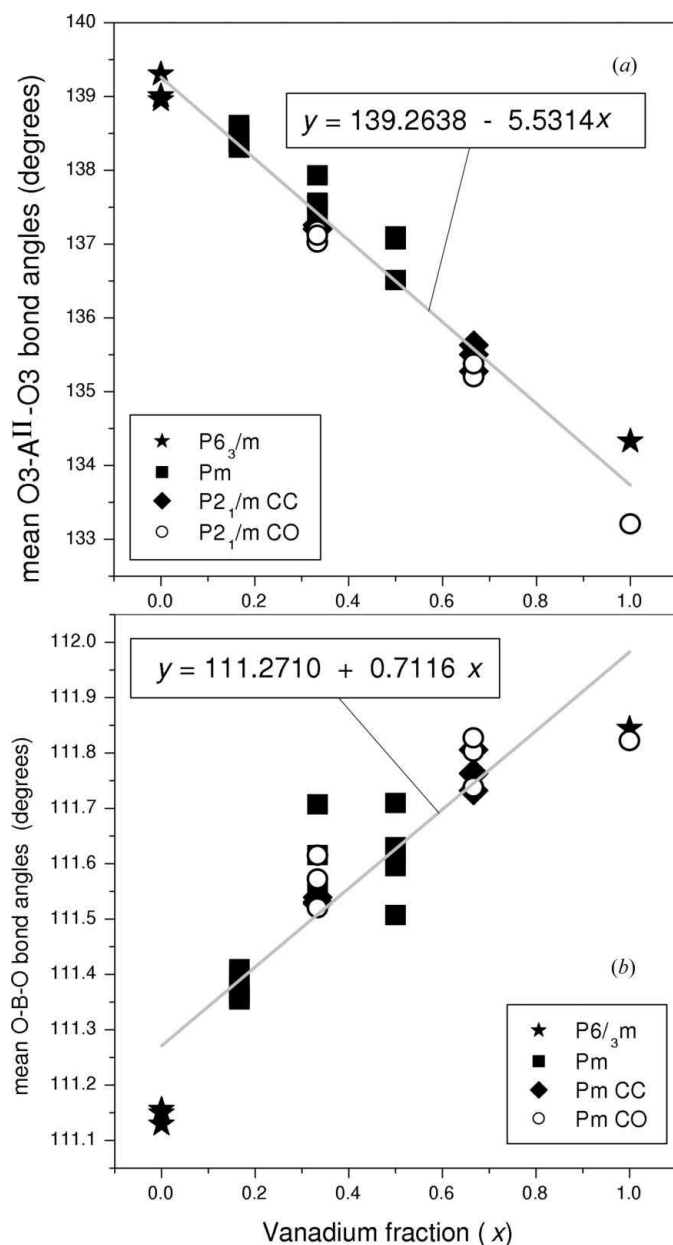

Figure 5
Mean values of (*a*) O3−A^{II}−O3 and (*b*) O−B−O oxygen–cation–oxygen bond angles for given *ab initio* structures as a function of the vanadium fraction x.

3.3. Direct least-squares refinement of crystal-chemical parameters

An initial attempt at simultaneous direct least-squares determination of all 10 crystal-chemical parameters yielded structures with reasonable bond distances and angles. However, SVD analysis of the least-squares normal equation matrix indicated that the τ_{O-B-O} and $\varphi_{O3-A^{II}-O3}$ bond-angle parameters (Table 2) were the main components of eigenvectors associated with small singular values, meaning that their standard uncertainty (s.u.) would be large and therefore that their numerical values would be extracted with poor precision. We accordingly performed tests where we imposed values for τ_{O-B-O} or $\varphi_{O3-A^{II}-O3}$. We observed that quite a large range of values could be imposed in this way with no meaningful change in residuals, goodness-of-fit or other agreement factors, but with clear repercussions for values extracted for the eight remaining parameters. This kind of behavior is presumably caused by the fact that the singular vectors are mostly but not entirely along the variables τ_{O-B-O} or $\varphi_{O3-A^{II}-O3}$. Imposed changes in the numerical values of those variables can then be compensated for by changes in other refinement variables, without a significant change in the agreement factors. Whatever its cause, this kind of behavior of the least-squares refinement is most worrying for the extraction of meaningful crystal-chemical parameters.

3.4. *Ab initio* optimized values for τ_{O-B-O} and $\varphi_{O3-A^{II}-O3}$

In order to better condition the crystal-chemical refinement, numerical values derived from *ab initio* total-energy minimization calculations (Table 3 – supplementary material) were imposed on the bond-angle parameters τ_{O-B-O} and $\varphi_{O3-A^{II}-O3}$. Selected bond distances and angles (Table 6 – supplementary material) for individual crystallographic sites of $P1m1$ and $P112_1/m$ *ab initio* optimized structures show that the mean O−B−O and O3−A^{II}−O3 oxygen–cation–oxygen bond angles display a linear behavior when plotted against the vanadium fraction x (Fig. 5).

3.5. *Ab initio* constrained crystal-chemical refinement

Imposing τ_{O-B-O} and $\varphi_{O3-A^{II}-O3}$ values from *ab initio* simulations produced stable crystal-chemical Rietveld analyses, *i.e.* normal least-squares matrices with condition numbers sufficiently high to ensure *precise and stable* evaluation of refinement variables (Mercier *et al.*, 2006*b*). Fig. 6 plots the eight crystal-chemical parameters (Table 7 – supplementary material) obtained by direct least-squares extraction for the solid-solution series by imposing values read off the linear relationships of Fig. 5 to bond-angle parameters $\varphi_{O3-A^{II}-O3}$ and τ_{O-B-O}. Note that Figs. 4 and 6 are shown on the same overall scales for the corresponding parameters.

4. Discussion

4.1. Electron diffraction and imaging

The large difference in ionic radii (Shannon, 1976) of tetrahedrally coordinated P^{5+} (0.17 Å) and V^{5+} (0.355 Å) raises the possibility of ordering, which in the simplest case of $Ca_{10}(PO_4)_3(VO_4)_3F_2$ would result in alternate phosphorus and
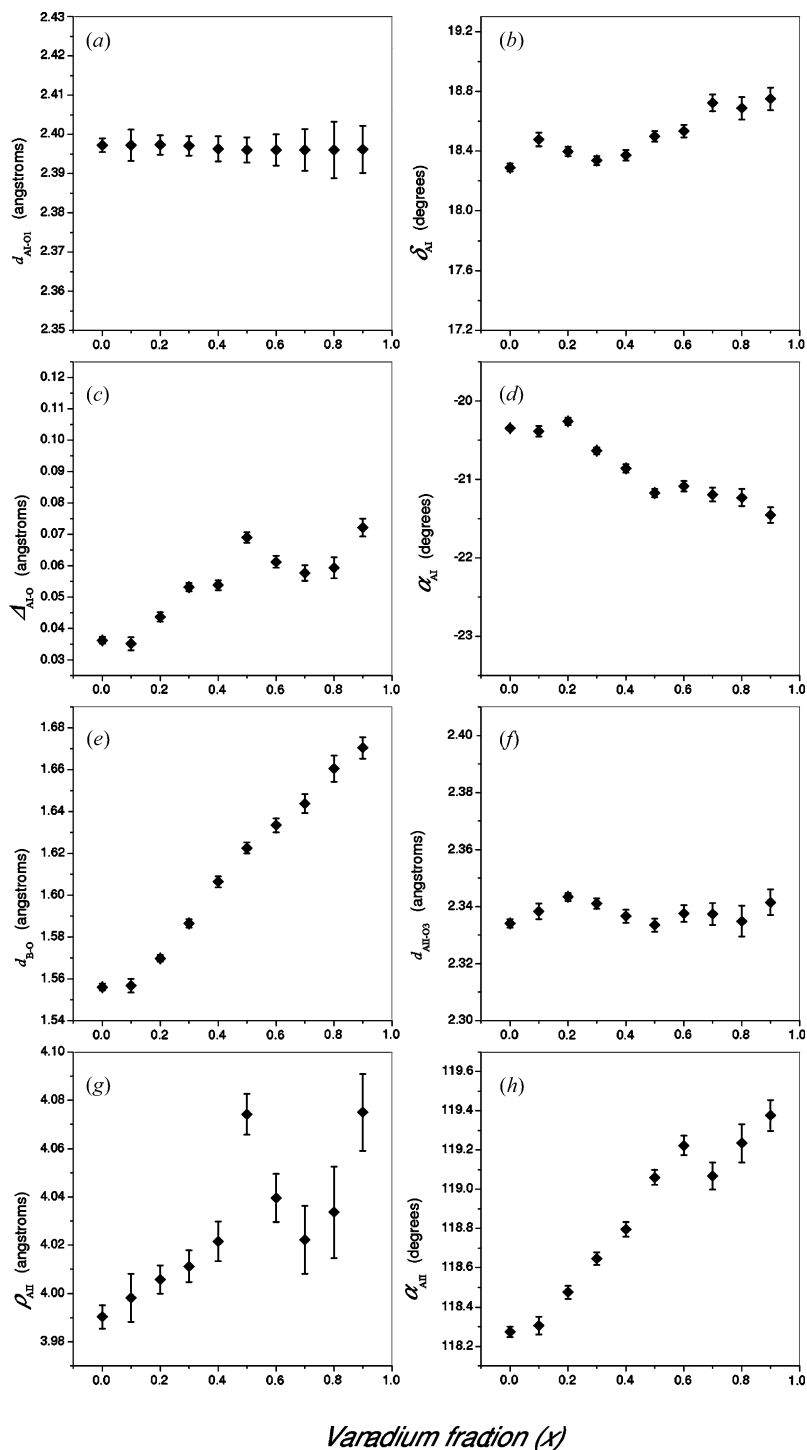

Figure 6
Crystal-chemical parameters (Table 7 – see supplementary material) obtained by direct least-squares extraction for the solid-solution series by imposing the linear relationships of Fig. 3 to bond-angle parameters $\varphi_{O3-A^{II}-O3}$ and τ_{O-B-O}.

vanadium in successive atomic planes perpendicular to the channels, an ordering which results in the space group $P\bar{6}$. In principle, this symmetry is readily distinguished from $P6_3/m$ in the [100] or [110] zone axes as $00l$, $l = 2n$, reflections will be absent only when the screw axis is present. However, in selected-area electron diffraction, the superposition of double diffraction reflections makes such analyses problematic, and convergent-beam electron diffraction that would limit this effect may be compromised by the reduction of V^{5+} and crystallographic alteration to perovskite under a focused electron beam (Dong *et al.*, 2005). Direct imaging of the tetrahedral sites also proves inconclusive, as simulations show the averaged projected potential of overlaid phosphorus and vanadium is indistinguishable in either the $P6_3/m$ or $P\bar{6}$ models (Fig. 2a). There remains the prospect that compositionally elicited nano-domains 50–1000 Å in extent may exist, as observed in natural apatite (Ferraris *et al.*, 2005) and plumbous vanadinites (Dong & White, 2004a). Domains were not detected in any samples, with the projected structures appearing to be very homogeneous – a typical example for the preparation of nominal composition $Ca_{10}((V_{0.5}P_{0.5})O_4)_6F_2$ is shown in Fig. 2(b). Similarly, the reduction of symmetry to $P2_1/m$ that was proposed earlier (Dong & White, 2004b) for $Ca_{10}(VO_4)_6F_2$ was not distinguishable by high-resolution imaging (Fig. 2c).

4.2. Crystal-chemical *versus* standard Rietveld refinement results

In comparing the systematics arising from crystallographic (Table 4 – supplementary material – Fig. 3) *versus* crystal-chemical (Table 7 – supplementary material, Fig. 6) Rietveld refinement, the most striking observations are as follows: First, inverse solid-solution systematics (Fig. 4c *versus* Fig. 6b) were extracted for the counter-rotation angle δ_{A^I} (Table 2, Fig. 7). The latter parameter is equivalent to the A^IO_6 metaprism twist angle φ ($\varphi = 60° - 2\cdot\delta_{A^I}$) first defined by White & Dong (2003). As a classification of the apatites based on the metaprism twist φ has been presented in White *et al.* (2005), it becomes important to ascertain which of the two sets of values extracted for δ_{A^I} are reliable. Fig. 7 compares the set values with the correlation δ_{A^I} *versus* $\varphi_{O3-A^{II}-O3}$ observed by Mercier, Le Page *et al.* (2005) for accurate single-crystal refinements and *ab initio* simulations of the known $P6_3/m$ end-member structures. It is shown that δ_{A^I} values extracted by crystal-chemical refine-
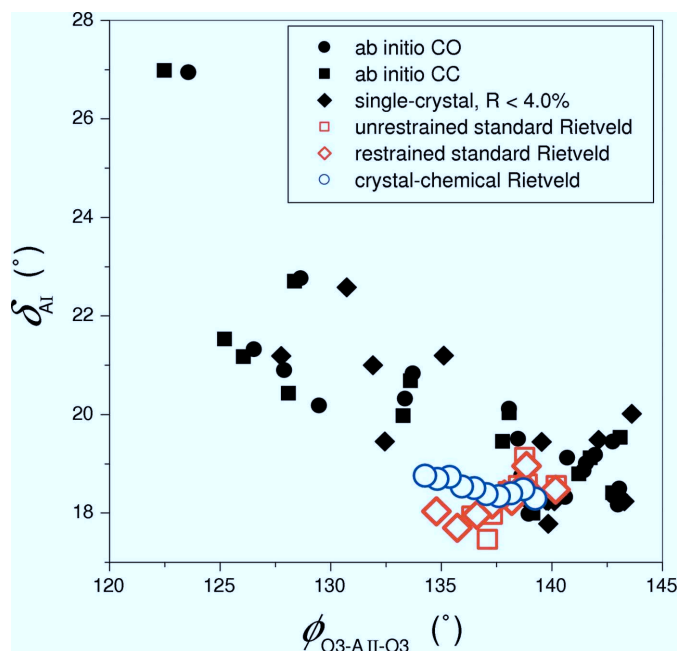
Figure 7
Comparison of δ_{A^I} values extracted by crystal-chemical *versus* standard crystallographic Rietveld refinements for the solid solution with the correlation δ_{A^I} *versus* $\varphi_{O3-A^{II}-O3}$ observed by Mercier *et al.* (2005) for accurate single-crystal refinements and *ab initio* simulations of the known $P6_3/m$ end-member structures.
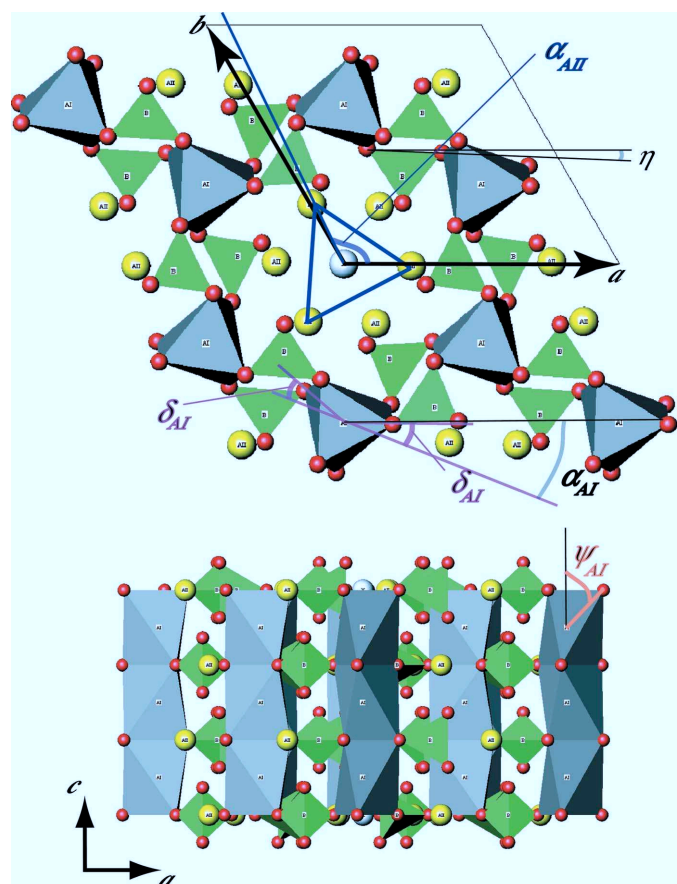

Figure 8
Diagrams showing the main geometric rearrangements that take place as more and more vanadium is substituted in the fluorapatite structure.

ment are in better general agreement with the trend in Mercier, Le Page *et al.* (2005) than those obtained from standard crystallographic refinement results. As the trend was established with intrinsically more accurate single-crystal data, it is concluded that the crystal-chemical refinement method provides a more accurate quantitative crystal-chemical analysis of the $A^I O_6$ metaprism twist angle than a standard refinement of the same data.

It is also observed that variations of interatomic distance parameters for calcium–oxygen bonds in the A^I and A^{II} sites are much larger in the standard refinements (Figs. 4a, b and i) than in their crystal-chemical counterparts (Figs. 6a, c and 6f). In comparing results from crystal-chemical *versus* standard crystallographic types of refinement using a high-quality fluorapatite X-ray powder data set, Mercier *et al.* (2006a) observed similar magnitudes of interatomic distance variations by performing numerous refinements of the same experimental data with the addition of artificial random intensity noise, indicating a precision which is nearly an order of magnitude greater for crystal-chemical refinement than for standard crystallographic Rietveld analysis. This means that the range of values extracted here for interatomic distance parameters involving calcium–oxygen bonds in the A^I and A^{II} sites, by both unrestrained and restrained standard Rietveld refinement, varies somewhat from data set to data set. On the other hand, crystal-chemical refinement results indicate only a small data-set-to-data-set variation across the solid solution for the bond-length difference Δ_{A^I-O} between A^I-O1 and A^I-O2 bonds, and almost no significant variation for the A^I-O1 and $A^{II}-O3$ bond lengths. As discussed below in §4.5, the apparent difficulty in quantitative evaluation of interatomic distances for calcium–oxygen bonds in A^I and A^{II} sites can be attributed to the poor precision in resolving oxygen positions
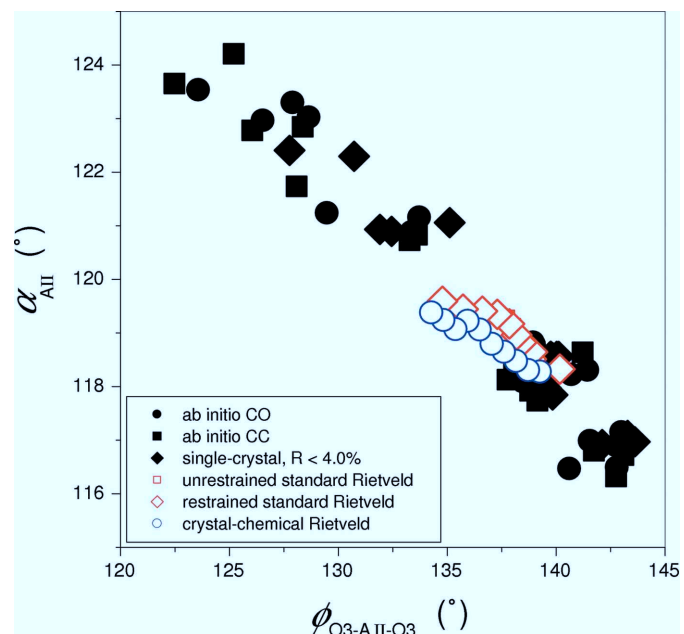

Figure 9
The angle $\alpha_{A^{II}}$ as a function of the $\varphi_{O3-A^{II}-O3}$ bond angle.

with conventional X-ray Rietveld refinement in the presence of heavy elements. The same remark applies to the lower accuracy in the determination of the $A^{\mathrm{I}}O_6$ metaprism twist angle φ by standard crystallographic refinement.
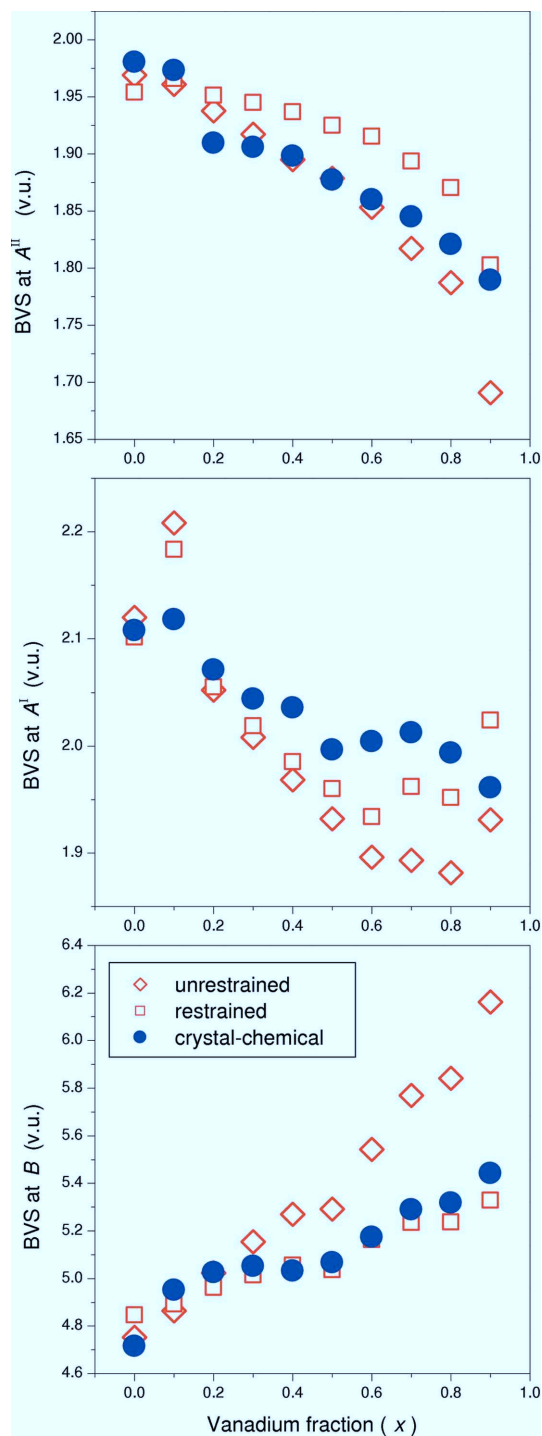

Figure 10
Bond-valence sums (BVS) at sites A^{I}, A^{II} and B (Table 8 – supplementary material) plotted as a function of the vanadium fraction x.

4.3. Crystal-chemical systematics of vanadium-substituted fluorapatites

The present analysis allows the systematic tracking of structural modifications in fluorapatite when phosphorus is progressively replaced by larger vanadium (Fig. 8). As the vanadium content increases, the concomitant geometric re-arrangements include:

(i) a rotation η (Fig. 8) and a uniform expansion of BO_4 tetrahedra that take place through a linear increase of the B—O bond lengths (Figs. 4e and 6e), accompanied by minor ($\sim 1°$) bending of O—B—O bond angles (Figs. 4f and 5b);

(ii) bond-stretching adjustment of the $Ca^{\mathrm{I}}O_6$ polyhedra (Figs. 4a and b, and 6a and c), which elongate through variation in the $\psi_{A^{\mathrm{I}}-O1}$ angle (Table 7 – supplementary material; Fig. 8), slightly twist through the counter-rotation angle $\delta_{A^{\mathrm{II}}}$ (Fig. 7) and rotate by an angle $\alpha_{A^{\mathrm{I}}}$;

(iii) an expansion of the edges of the Ca—Ca—Ca triangles $\rho_{A^{\mathrm{II}}}$ (Figs. 4g and 6g) and rotation away from the BO_4 tetrahedra through $\alpha_{A^{\mathrm{II}}}$ (Fig. 8). The angle $\alpha_{A^{\mathrm{II}}}$ progressively increases towards a value of 120° for large vanadium contents (Figs. 4h and 6h).

By plotting the angle $\alpha_{A^{\mathrm{II}}}$ as a function of the $\varphi_{O3-A^{\mathrm{II}}-O3}$ bond angle (Fig. 9) for *ab initio* simulation results and published single-crystal work of a wide selection of $P6_3/m$ apatite end-members, it was found that there is a gap at around $\alpha_{A^{\mathrm{II}}} = 120°$ in an otherwise dense plot (Mercier, Le Page *et al.*, 2005). In terms of the present experiments, it is significant that the observed $\alpha_{A^{\mathrm{II}}}$ values for the phosphorus–vanadium solid solution (Figs. 4g and 6h) move inside this gap as the vanadium content increases. In addition, the refinements show that:

(i) the refined microstrain parameters (Tables 2 and 4 from the supplementary material) for $Ca_{10}(V_xP_{1-x}O_4)_6F_2$ samples with $x = 0.0$–0.9 correlate directly with the vanadium fraction x; and

(ii) the X-ray powder pattern for the $Ca_{10}(VO_4)_6F_2$ end-member is clearly of lower-symmetry, in line with previous work (Kreidler & Hummel, 1970; Dong & White, 2004b).

It is proposed, therefore, that as the $\alpha_{A^{\mathrm{II}}}$ angle approaches 120° for large vanadium content, a lowering of the symmetry is induced. The steady trend in refined strain parameters *versus* vanadium content, as opposed to a maximum around $x = 0.5$ composition that is expected for solid solutions, is presumably an additional indication of the nearby symmetry transformation.

4.4. Promoting symmetry reduction of metal-substituted fluorapatites

An empirical analysis of the driver for a phase transformation to lower symmetry can be gained by considering the bond-valence sums (BVS) at the sites A^{I}, A^{II} and B (Fig. 10, Table 8 – supplementary material). For the pure phosphate, Ca^{2+} fits neatly in the A^{II} site with a BVS of +2 v.u. (valence units), while it is somewhat compressed at site A^{I} (BVS > +2 v.u.). As the vanadium content increases, the bond length of the BO_4 tetrahedron increases as expected (Figs. 4e and 6e),

and causes a parallel increase in the average metal–anion bond length ($\langle M-A \rangle$) of the A^{I} and A^{II} sites (Table 8 – supplementary material). At the highest vanadium contents, just prior to the phase change in the $Ca_{10}(VO_4)_6F_2$ end-member, Ca^{2+} matches the A^{I} site interstice, while it is now somewhat small for the expanded A^{II} site (BVS < +2 v.u.). Similarly, the tetrahedral B site is slightly stretched at the P end-member (BVS < 5 v.u.) and quite compressed (BVS > 5 v.u.) just before the symmetry change at the V end-member. While these departures from ideal valences are not unexpected, the deviations of the BVS observed at the A^{II} and B sites become exceptionally large at high vanadium content. This suggests that the phase transformation is promoted by the need to relax O atoms toward A^{II} sites and away from B sites. A bond-valence analysis of the monoclinic $P112_1/m$ model for $Ca_{10}(VO_4)_6F_2$ in Dong & White (2004b) indeed indicates significant relaxation at the V site, and to a lesser degree at the A^{II} site, although further work is needed to establish the generality of this interpretation.

As valence summation indicates extension stress on the A^{II} site in the vanadate-rich region, it follows that divalent ions of radius slightly larger than Ca^{2+}, such as Pb^{2+}, would preferentially occupy the A^{II} site and stabilize the hexagonal phase by reducing the stress on site A^{II}. This rationalization appears to be qualitatively supported by experiment as Pb^{2+} in $(Pb_xCa_{10-x})(VO_4)_6F_2$ (Dong & White, 2004a,b) is seen to both preferentially occupy A^{II} and stabilize the hexagonal $Pb_{10}(VO_4)_6F_2$ end-member.

4.5. Complementarity of quantum methods and structure analysis by X-ray powder diffraction

Although the observations made here apply specifically to the Rietveld extraction of the crystal chemistry of vanadium-substituted fluorapatites, the approach is generally applicable to Rietveld refinements of moderately complex metal-oxide systems. SVD analysis of the normal matrix of Rietveld least-squares (Mercier et al., 2006b) indicates that singular values associated with some variables or singular combinations of variables are small, both for standard crystallographic refinement and for crystal-chemical refinement (Mercier et al., 2006a). These singular values are the inverse of the variance of the corresponding variable or combination of variables, which means that some aspects of geometry and therefore crystal chemistry will be determined imprecisely. With standard crystallographic refinement of metal oxides with sealed-tube X-ray data, the O-atom coordinates are presumably in a category of variables associated with eigenvectors having weak eigenvalues compared with those of eigenvectors corresponding to unit-cell parameters and heavy-element coordinates. As the crystal chemistry of metal oxides is rationalized in terms of distortions and rotations of oxide polyhedra, it follows that the crystal chemistry extracted by crystallographic Rietveld refinement of conventional X-ray data will inevitably be compromised by the inherent difficulty in refining the oxygen coordinates demonstrated by SVD

analysis of refinement matrices. While crystal-chemical refinements also include combinations of variables with small singular values, there are fewer of them compared with standard crystallographic refinements, but the extracted crystal chemistry is only marginally superior. Extraction of useful crystal chemistry by Rietveld profile analysis of sealed-tube X-ray data from metal oxides should therefore be performed with caution.

Reliability can be enhanced by considering that in crystal-chemical refinements all crystal-chemical variables are algebraically independent in the model, but do not have the same degree of interpretability. Metal–oxygen distances are often interpreted in terms of bond valence (Brown & Altermatt, 1985) or by comparison with tables of ionic radii (Shannon, 1976). In the same way, polyhedral rotations may be intuitively understood in terms of steric effects within the structure. However, crystal-chemical instinct is often insufficient for rational interpretation of oxygen–cation–oxygen bond angles. In the case of apatite, the introduction of such crystal-chemical parameters in the model was essential to establish algebraic equivalence with the crystallographic description of the structure. Fortunately, bond angles and polyhedral rotations are accurately reproduced by ab initio optimization of the corresponding structure models, as demonstrated through comparisons with published accurate single-crystal work (Mercier, Le Page et al., 2005). A rational approach then is to fix one or more of those oxygen–metal–oxygen angles at values calculated through ab initio modeling, in order to better condition the Rietveld refinement. Hopefully, this would in turn allow the extraction of useful experimental values for the remaining crystal-chemical variables from conventional X-ray powder diffraction data.

The present study is a successful application of this procedure to combine the strengths of a variety of methods in different steps in the derivation. Instead of extracting metal–oxygen distances and angles from the poorly determined variables of standard crystallographic refinements, crystal-chemical refinement considers interatomic distances and angles to be variables in their own right, thus decreasing the possibility of incorrect derivation. It is well known that density-functional theory (DFT) quantum modeling may not be adequate to accurately determine bond lengths because the numerical accuracy of ab initio 'potentials' used to describe the electronic core is not yet quite sufficient for this purpose. However, DFT has proved reliable at modeling small structural adjustments, as shown by the success of the quantum extraction of elastic tensor coefficients (see e.g. Le Page & Rodgers, 2005, and references therein), as this method establishes with considerable accuracy the minimum-energy configuration of valence electrons through hybridization of electronic orbitals. It is this hybridization that controls the bond-bending or polyhedral-rotation angles of the type that cannot be precisely obtained by Rietveld refinement of data from a sealed X-ray tube. In summary, this asset of DFT modeling can be used to compensate for the corresponding limitation of X-ray refinement, leading to better-conditioned crystal structure determinations, providing a route for the

derivation of more precise experimental values for the refinement variables that the crystal chemist needs most.

It can be argued that the more precise values derived in this way are somewhat less experimental than other values derived by full refinement of all possible variables in a standard crystallographic refinement, including atom occupancies, anisotropic atom displacements, extinction *etc*. The results of such unbiased refinements on our measured Cu $K\alpha$ powder data sets would also have been inappropriate for the purpose of correctly extracting the crystal chemistry. This is because the imprecision of O-atom coordinates would have been made worse by the introduction of additional refinement parameters, leading to inconclusive results. Treatment of standard refinement analogous to the procedure we have followed for crystal-chemical refinement would probably have resulted in our accepting metal positions from the X-ray Rietveld refinement while imposing O-atom positions from DFT optimization. For the extreme case where all oxygen coordinates would have been imposed in this way to obtain a stable and precise evaluation of remaining refinement variables, the extracted crystal chemistry could then hardly be called experimental because it would mostly be from DFT calculations. In this regard, the *ab initio* constrained crystal-chemical refinement approach developed here is then a way to extract as much experimental crystal chemistry as possible, but the Cu $K\alpha$ X-ray powder profile we could produce was still borderline. Under the circumstances, it seemed justified to have made the few simplifying and plausible assumptions detailed above, the reason being that these assumptions ended up making the difference between an unbiased but also inconclusive study and the plausibly constrained conclusive experimental crystal-chemical results reported here.

The remaining freely refined crystal-chemical parameters extracted from experimental profile measurements in no way contradict the DFT model optimized from theory. In other words, we almost reached the goal of most experiments: to perform a measurement, interpret it with a model in the light of existing theory down to the precision of the measurement and to derive useful conclusions from this interpretation. If we accept that the precision of the measurements is indicated by the agreement factors obtained with standard refinement of the same data, we have essentially achieved that goal of exhausting the precision in the data with a model that agrees with theory. Experimental results and those of DFT computations buttress each other here and reinforce our trust both in the conclusions of the experimental study and in the soundness of the principles and approximations at the root of DFT software. It has helped significantly to be able to stabilize a least-squares system with partial results from DFT theory, and then observe agreement between theory and experiment over the remaining refinement parameters within the limitations of each approach. Known current deficiencies of DFT are not built into the method and there is progress each year in this area. It is currently too early to attempt to derive from theory alone structural information that can also be extracted experimentally. We nevertheless trust that, similar to what is already happening with the elasticity of materials (see *e.g.* Le

Page & Rodgers, 2005, and references therein), the day will come for the design work of materials because computations are already much cheaper than experiment for moderately large systems. The present study is hopefully a step in that direction.

5. Conclusions

By imposing results of quantum modeling in a crystal-chemical Rietveld refinement, a precise description of the vanadium-substituted fluorapatites has been obtained. Replacement of P^{5+} by V^{5+} is accommodated primarily by uniform expansion and rotation of BO_4 tetrahedra combined with a rotation of the Ca—Ca—Ca triangular units through the angle $\alpha_{A^{II}}$ defined in Mercier, Le Page *et al*. (2005). It is postulated that the reduction of symmetry for vanadium-rich apatite arises because:

(i) the angle $\alpha_{A^{II}}$ for the solid solution approaches a value of $120°$; and

(ii) significant departures from formal valence at the A^{II} and B sites occur.

The novel approach of combining crystal-chemical Rietveld refinement and quantum calculations developed and implemented here is in general well suited for the precise investigation of the crystal chemistry of metal oxide compounds and their solid solutions.

References

Brown, I. D. & Altermatt, D. (1985). *Acta Cryst.* B**41**, 244–247.
Bruker (2005). *TOPAS*, Version 3.0. Bruker AXS, Karlsruhe, Germany.
Cheary, R. W. & Coelho, A. (1992). *J. Appl. Cryst.* **25**, 109–121.
Cheary, R. W. & Coelho, A. (1998*a*). *J. Appl. Cryst.* **31**, 851–861.
Cheary, R. W. & Coelho, A. (1998*b*). *J. Appl. Cryst.* **31**, 862–868.
Crannell, B. S., Eighmy, T. T., Krzanowski, J. E., Eusden Jr, J. D., Shaw, E. L. & Francis, C. A. (2000). *Waste Manage.* **20**, 135–148.
Davidson, E. R. (1983). *Methods in Computational Molecular Physics*, edited by G. H. F. Diercksen & S. Wilson, Vol. 113, NATO Advanced Study Institute, Series C, p. 95. New York: Plenum Press.
Dong, Z. & White, T. J. (2004*a*). *Acta Cryst.* B**60**, 138–145.
Dong, Z. & White, T. J. (2004*b*). *Acta Cryst.* B**60**, 146–154.
Dong, Z., White, T. J., Sun, K., Wang, L. M. & Ewing, R. C. (2005). *J. Am. Ceram. Soc.* **88**, 184–190.
Dong, Z., White, T. J., Wei, B. & Laursen, K. (2002). *J. Am. Ceram. Soc.* **85**, 2515–2522.
Eighmy, T. T., Crannell, B. S., Krzanowski, J. E., Butler, L. G., Cartledge, F. K., Emery, E. F., Eusden Jr, J. D., Shaw, E. L. & Francis, C. A. (1998). *Waste Manage.* **18**, 513–524.
Ewing, R. C. & Wang, L. (2002). *Reviews in Mineralogy and Geochemistry*, Vol. 48, *Phosphates: Geochemical, Geobiological, and Materials Importance*, edited by M. J. Kohn, J. Rakovan & J. M.

Hughes, pp. 673–700. Mineralogical Society of America and Geochemical Society, Washington, DC.

Ferraris, C., White, T. J., Plévert, J. & Wegner, R. (2005). *Phys. Chem. Miner.* **32**, 485–492.

Kern, A., Coelho, A. A. & Cheary, R. W. (2004). *Diffraction Analysis of the Microstructure of Materials*, edited by E. Mittemeijer & P. Scardi, pp. 17–50. Berlin: Springer-Verlag.

Kim, J. Y., Dong, Z. & White, T. J. (2005). *J. Am. Ceram. Soc.* **88**, 1253–1260.

Kreidler, E. R. & Hummel, F. A. (1970). *Am. Mineral.* **55**, 170–184.

Kresse, G. (1993). PhD thesis. Technische Universita Wien, Austria.

Kresse, G. & Hafner, J. (1993). *Phys. Rev. B*, **48**, 13115–13118.

Kresse, G. & Hafner, J. (1994). *Phys. Rev. B*, **49**, 14251–14269.

Kresse, G. & Joubert, J. (1999). *Phys. Rev. B*, **59**, 1758–1775.

Le Page, Y. & Rodgers, J. (2005). *J. Appl. Cryst.* **38**, 697–705.

Mercier, P. H. J., Le Page, Y., Whitfield, P. S. & Mitchell, L. D (2006a). *J. Appl. Cryst.* **39**, 369–375.

Mercier, P. H. J., Le Page, Y., Whitfield, P. S. & Mitchell, L. D (2006b). *J. Appl. Cryst.* **39**, 458–465.

Mercier, P. H. J., Le Page, Y., Whitfield, P. S., Mitchell, L. D., Davidson, I. J. & White, T. J. (2005). *Acta Cryst.* B**61**, 635–655.

Mercier, P. H. J., Whitfield, P. S., Mitchell, L. D., Davidson, I. J., Le Page, Y. & White, T. J. (2005). *Advances in Ecomaterials – 7th International Conference on Ecomaterials (ICEM7) and 3rd International Conference on Materials for Advanced Technologies (ICMAT 5005)*, edited by T. White *et al.*, Vol. 2, pp. 396–401. Singapore: Stallion Press (S) Pte Ltd.

Methfessel, M. & Paxton, A. T. (1989). *Phys. Rev. B*, **40**, 3616–3621.

Monkhorst, H. J. & Pack, J. D. (1976). *Phys. Rev. B*, **13**, 5188–5192.

Shannon, R. D. (1976). *Acta Cryst.* A**32**, 751–767.

Stadelmann, P. A. (1987). *Ultramicroscopy*, **21**, 131–146.

Terra, O., Dacheux, N., Audubert, F. & Podor, R. (2006). *J. Nucl. Mater.* **352**, 224–232.

Valsami-Jones, E., Ragnarsdottir, K. V., Putnis, A., Bosbach, D., Kemp, A. J. & Gressey G. (1998). *Chem. Geol.* **151**, 215–233.

Vance, E. R., Ball, C. J., Begg, B. D., Carter, M. L., Day, R. A. & Thorogood, G. J. (2003). *J. Am. Ceram. Soc.* **86**, 1223–1225.

White, T. J. & Dong, Z. (2003). *Acta Cryst.* B**59**, 1–16.

White, T. J., Ferraris, C., Kim, J. & Madhavi, S. (2005). *Apatite – An Adaptive Framework Structure, in Reviews in Mineralogy and Geochemistry*, Vol. 57, *Micro- and Mesoporous Mineral Phases*, edited by G. Ferraris & S. Merlino, pp. 307–373. Mineralogical Society of America and Geochemical Society, Washington, DC.